ARTICLE

Study of the Interface between Rhodium and Carbon Nanotubes

Irene Suarez-Martinez,[†] Christopher P. Ewels,[†] Xiaoxing Ke,[‡] Gustaaf Van Tendeloo,[‡] Sebastian Thiess,[§] Wolfgang Drube,[§] Alexander Felten,[⊥] Jean-Jacques Pireaux,[⊥] Jacques Ghijsen,[⊥] and Carla Bittencourt[∥,*]

[†]IMN, Université de Nantes, CNRS, 2 rue de la Houssinière, BP32229, 44322 Nantes, France, [‡]EMAT, University of Antwerp, B-2020 Antwerp, Belgium, [§]HASYLAB am Deutschen Elektronen-Synchrotron DESY, D-22603 Hamburg, Germany, [⊥]PMR LISE, University of Namur (FUNDP), B-5000 Namur, Belgium, and [∥]LCIA, University of Mons, B-7000 Mons, Belgium

ABSTRACT X-ray photoelectron spectroscopy at 3.5 keV photon energy, in combination with high-resolution transmission electron microscopy, is used to follow the formation of the interface between rhodium and carbon nanotubes. Rh nucleates at defect sites, whether initially present or induced by oxygen-plasma treatment. More uniform Rh cluster dispersion is observed on plasma-treated CNTs. Experimental results are compared to DFT calculations of small Rh clusters on pristine and defective graphene. While Rh interacts as strongly with the carbon as Ti, it is less sensitive to the presence of oxygen, suggesting it as a good candidate for nanotube contacts.

KEYWORDS: metal−carbon nanotube interaction · interface · nucleation · rhodium · carbon nanotubes

As conventional complementary metal oxide semiconductor (CMOS) technology reaches its scaling limits, alternatives such as carbon nanotube (CNT)-based electronics have been extensively explored due to their high carrier mobility, ballistic transport, and high current capability when used in conjunction with high-K dielectric materials.[1−4] The reduction of dimensionality of interconnects in these new systems leads to electrical contacts with the contact formation chemistry determining to a great extent their electrical performance. Various metals have been investigated as possible candidates for electrical contact with CNTs.[5,6] Experimental results and calculations agree that Ti and Pd are the best candidates, superior to conventional metals previously used in microelectronics such as Au, Cu, and Pt, which form electrical contacts with high-resistance Schottky barriers when used to contact carbon-based nanostructures.[7] However, recent studies have shown that rhodium is capable of forming high-quality electrical contacts.[8] Kim *et al.* examined single-walled carbon nanotube field-effect transistors (SWCNT FETs) fabricated using Rh as an electrical contact material. They found that transistor behavior was largely constant without random fluctuation between devices once the diameters of the nanotubes were known. This allowed a systematic investigation of the dependence of Schottky barrier heights at the contacts between Rh and CNTs.

Creating Ohmic contacts on very small diameter ($d \leq 1$ nm) nanotubes is currently a key challenge and requires a strategy for eliminating the large tunnel barriers associated with small diameter SWCNTs. Understanding the interaction between Rh and the CNT surface is an important step toward achieving this goal. Larciprete *et al.* reported that Rh atoms evaporated onto CNT surfaces predominantly arrange in (111)-terminated three-dimensional clusters.[9,10] These authors showed that chemisorption of oxidizing species on the Rh clusters led to changes in the electronic structure of the interface at the metal−nanotube contact. The magnetic behavior of Rh monolayers on graphite has been studied theoretically using tight-binding methods,[11] as well as single-atom absorption on semiconducting single-walled nanotubes.[12]

The chemical behavior of graphitic carbon materials is predominantly influenced by the presence of defects.[13] For CNTs, nonhexagonal carbon rings, edges, and vacancies are sites of high-energy defects, that is, sites at which electron transfer takes place, hence making them much more chemically reactive than the perfect surface. The reaction of oxygen at defects and the thermodynamic and kinetic parameters affecting the formation of oxo groups have been extensively studied both theoretically and experimentally.[14,15] Typically, the number of oxo groups which naturally graft at the CNT surface due to interaction with atmospheric oxygen is too low to be chemically

*Address correspondence to carla.bittencourt@umh.ac.be.

Received for review November 11, 2009 and accepted February 12, 2010.

Published online February 18, 2010. 10.1021/nn9015955

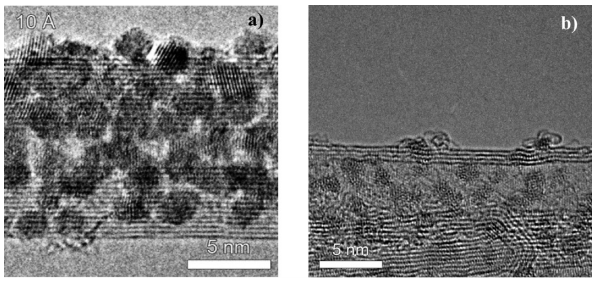

Figure 1. HRTEM image of (a) Rh clusters on a CNT, revealing the Rh atomic planes and the preserved CNT structure. (b) Formation of small-ordered fullerene-like protrusions attached to Rh particles.

significant. Therefore, several methods have been used to create reactive chemical sites and introduce oxo groups onto CNT surfaces in a controlled manner, among which oxygen-plasma treatment was shown to be an effective method. The effect of various plasma preparation parameters on the number, nature, and relative distribution of oxo groups on carbon and the CNT surface has been studied in detail by several groups.[16−18]

In order to understand the Rh nucleation mechanism on imperfect CNT surfaces, we evaporated different amounts of Rh onto the surface of pristine and oxygen-plasma-treated multi-walled carbon nanotubes (MWCNTs), which were analyzed using transmission electron microscopy (TEM) and X-ray photoelectron spectroscopy (XPS) at a photon energy of 3.5 keV. The experimental results were compared to density functional (DFT) calculations of the interaction between Rh atoms and pristine and defective graphene.

RESULTS AND DISCUSSION

Figure 1a shows a HRTEM image of Rh deposition on a pristine tube, demonstrating a preserved interface and crystalline ordering within the Rh particles. This result can be understood in the context of DFT calculations. On a graphitic surface, our calculations show that single Rh atoms prefer to reside above a hexagon center with 3.22 eV binding energy (Figure 2). Compared to the other metals we have studied (Ti, Ni, Pd, Pt, and Au), this is the strongest binding in agreement with reports.[19−21] The system has a net magnetic moment of 1.0 μ_B with an average C−Rh distance of 2.24 Å, with the Rh atom sitting 1.71 Å above the graphitic layer. When maintaining the same spin, neither above a carbon atom nor over a C−C bond are sites stable (0.42 and 0.35 eV less stable than the ground state, respectively). This is in contrast to the work of Zhao *et al.*[12] who, for model semiconducting (8,0) nanotubes, found a preference for Rh to reside above bond-centered sites, with a binding energy of 2.48 eV and a shorter bond length (2.09 Å). There are a number of differences in the calculations (for example, they used the generalized gradient approximation (GGA) for exchange and correlation, with a smaller basis set), but we suspect the primary difference is due to the high curvature and semiconducting band gap of the (8,0) nanotube, as compared to the graphene used for our modeling and the large-radius multi-walled nanotubes used in the experiments presented here.

Our calculated binding site values provide a minimum migration barrier of 0.35 eV for Rh diffusion on the graphitic surface over bond-centered sites. This means Rh will be surface mobile at room temperature, unlike Ti,[22] although slower moving than Pd, Pt, or Au,[23] consistent with experimental observations of Rh deposition on HOPG.[28] This lower surface mobility of Rh as compared to Au can be seen in a much more even size distribution of clusters as compared to Au, with smaller average particle sizes[23] (see Figure 4).

Our calculations suggest that Rh will preferentially form 3D clusters on the graphitic layer rather than wetting the surface: a tetrahedral configuration for Rh_4 is 0.38 eV more stable than the planar configuration when attached to the graphitic surface (the converse is true for Ti).[22] Although this may at first sight appear contradictory with the high binding energy that we found for single Rh atoms on graphite, the tendency to cluster comes from the high cohesive energy of Rh. These calculations explain the difference in surface behavior between Rh and Ti, which shows energetic preference for uniform surface coverage and is surface immobile at room temperature, resulting in uniform amorphous surface coverage.[22] Rh, however, energetically prefers clustering and is sufficiently surface mobile to facilitate this. This can be seen in the HRTEM image in Figure 1a, showing Rh deposition on a pristine tube. The observa-

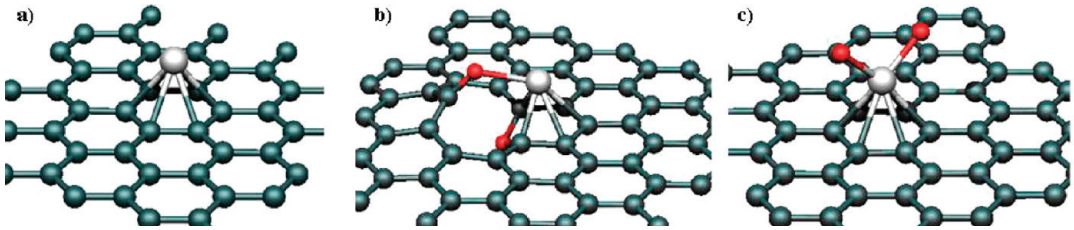

Figure 2. (a) Single Rh atom sitting above a hexagon site, similar to Ti. (b) Single Rh atom bonded to a vacancy O_2 defect. The ketone-bonded oxygen forms a C−O−Rh bridge, while the ether-bonded oxygen is deflected away with dilated bonds. The energetic cost to displace this ether oxygen to sit above the Rh (effectively exchanging positions with the Rh) is only 0.67 eV. (c) Rh reacts with an O_2 molecule to give a RhO_2 species which sits further from the graphene sheet than isolated Rh.

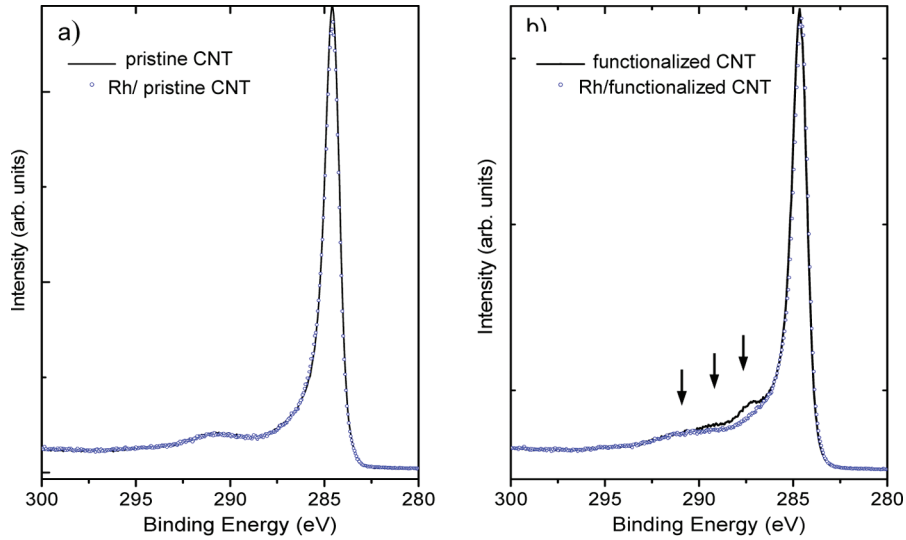

Figure 3. Comparison of the C 1s core-level XPS spectrum recorded on (a) pristine CNTs coated with a nominal amount of 5 Å Rh. (b) Plasma-functionalized CNTs and coated plasma-functionalized CNTs with a nominal amount of 5 Å Rh.

tion of the Rh atomic planes and the preserved interface suggests a stronger self-interaction within the Rh cluster than with the CNT surface, as well as local crystalline ordering of the Rh atoms.

Goldoni *et al.* showed that Rh atoms evaporated on a flat clean HOPG surface at room temperature have high mobility forming 3D islands, while Rh atoms can bind relatively strongly to defects at the HOPG surface.[28] With the aim of analyzing Rh nucleation in the presence of defects at the CNT surface, CNTs were oxygen-plasma-treated before Rh deposition. Within the volume analyzed by XPS, 16% of all atoms are oxygen atoms. Figure 3 shows XPS spectra for the C 1s peak recorded on pristine and oxygen-plasma-treated CNTs, before and after Rh evaporation. In the pristine samples, the C 1s spectrum has its main feature at 284.3 eV and a secondary, the core-energy-loss spectrum, near 291 eV corresponding to a p plasmon excitation. After the oxygen functionalization, a shoulder can be observed at the high-energy side of the C 1s peak; this shoulder is generated by photoelectrons emitted from C atoms in oxo groups: hydroxyl (component centered at 286.2 eV), carbonyl (or ether) (component centered at 287.2 eV), and carboxyl (or ester) groups (component centered at 288.9 eV).[24] Thus, the oxygen-plasma treatment resulted in the grafting of oxo groups at the chemically inactive surface of the CNTs.

In Figure 4a,b, the TEM images show the result of Rh evaporation onto pristine and oxygen-plasma-treated CNTs. The evaporation was performed simultaneously on both samples, ensuring that the same amount of metal was evaporated on each sample. At both pristine and plasma-treated CNT surfaces, clusters are formed, similar to the three-dimensional island formation observed in the calculations above and those seen when Rh is evaporated onto graphite at room temperature.[25] Better cluster dispersion and smaller contrast ratio is observed for the plasma-treated sample. Figure 4 shows the typical Rh cluster size distribution evaluated on pristine and oxygen-plasma-treated CNTs. It can be seen that after plasma treatment the maximum of the size distribution curve shifts from ~15 to 11 Å, and the particle sizes are more uniform. These results suggest that plasma treatment of the CNT surface creates oxidized dispersed vacancies, which reduce the size and size distribution of the Rh clusters while increasing the overall surface coverage. Comparing panels a and b of Figure 4, an amorphous layer can be seen on the pristine CNTs in the regions surrounding the Rh particles; for plasma-functionalized samples, this effect is reduced. We suggest that the formation of the amorphous layer is an electron beam effect. Under electron beam irradiation, carbon atoms adsorbed at the CNT surface can desorb or surface migrate and interact with the Rh particles, forming the amorphous layer. Closer investigation of this layer (Figure 1b) shows fullerene-like obtrusions attached to Rh particles. We suggest these are formed through local ordering induced by the electron beam, but they nonetheless raise the interesting possibility of Rh as a catalyst for nanotube growth.

For our calculations, we chose oxygenated vacancies as a representative defect for oxygen-plasma damage, as they contain both C═O and C−O−C functional groups.[30] A single Rh atom binds 0.86 eV more strongly with an oxygenated vacancy (binding energy 4.08 eV) than with perfect graphene (binding energy 3.22 eV), and thus, oxygenated vacancies will act as pinning sites for Rh atoms. Since the density of nucleation sites created during the oxygen-plasma treatment is high, diffusion-limited aggregation cannot describe the nucleation process. Instead, the growth is influenced by nucleation taking place in the proximity of oxygenated defects created during the oxygen plasma.

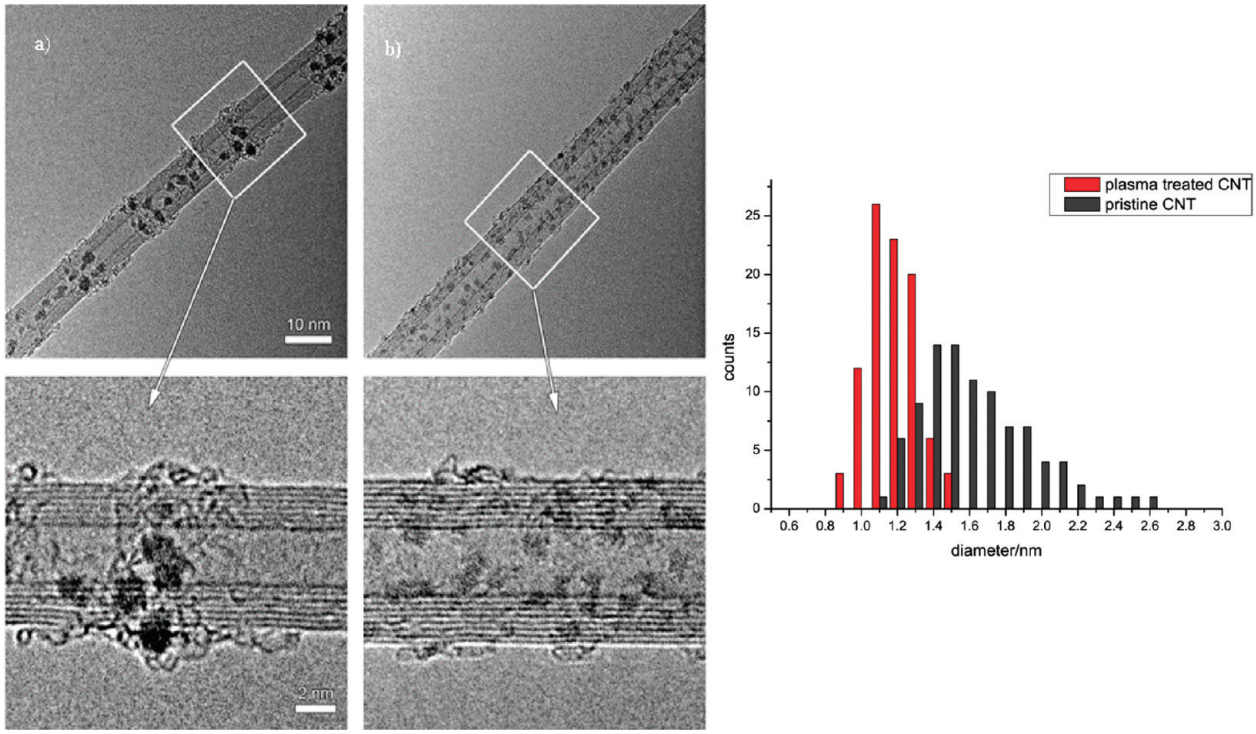

Figure 4. TEM images of Rh on (a) pristine and (b) oxygen-plasma-treated MWCNTs (nominal Rh evaporation of 1 Å). Graph: Rh cluster size distribution on pristine and oxygen-plasma-treated CNTs. Nominal Rh evaporation of 1 Å.

Comparison of the line shapes of the C 1s XPS spectrum recorded before and after evaporation of 1 Å Rh onto pristine and plasma-treated CNTs showed no additional structures, suggesting that no strong Rh−C bonds were formed (Figure 3). However, for plasma-treated CNTs the C 1s satellite peaks due to oxo groups are reduced after the Rh evaporation (Figure 3b). Two effects can contribute to this observed reduction. First, photoelectrons emitted from C atoms beneath the Rh clusters will experience inelastic losses when passing through the metal and thus no longer contribute to the C 1s main peak. If Rh selectively covers oxygen-rich (defective) areas, this will selectively reduce intensity from oxygen-related C 1s satellite peaks. Comparison of the O 1s XPS spectra recorded before and after Rh deposition reveals a new chemically shifted component at the low-energy side of the peak (Figure 5), indicative of interaction of the Rh clusters with oxygenated defects.[7] This confirms that the improvement in Rh cluster dispersion for the plasma-treated CNTs is associated with the presence of homogeneously distributed oxidized defects at the CNT surface, while the smaller cluster size can be linked to the increased number of nucleation centers.

A second possible cause for the reduction in oxygen-related C 1s satellite peaks in the XPS is the formation of O−Rh bonds at the expense of C−O bonds. C−O−Rh bonding will change the screening of the C−O bonds, thereby changing the binding energy of their C 1s levels. The chemically shifted component in the O 1s spectrum is consistent with strong Rh−O interaction (Figure 4). Our calculations show that a single Rh atom bonds to the ketone-bonded oxygen atom of an oxygenated vacancy, forming a Rh−O−C bridge, with a Rh−O distance of 2.05 Å and a C−O bond of 1.27 Å, dilated from 1.22 Å in the absence of Rh (see Figure 1b). The Rh resides on a hexagon center site displaced toward the oxygen. However, the Rh also interacts strongly with the neighboring ether-bonded C−O−C oxygen atom, displacing it downward, with a Rh−O distance of 2.54 Å and C−O bonds of 1.43 Å (a 5% dilation due to the presence of Rh). The defect center has zero spin. If we modify the structure so that Rh displaces the ether-bonded oxygen out of the vacancy, the resultant relaxed structure is only 0.67 eV less stable than the ground-state structure described above (*i.e.*, still

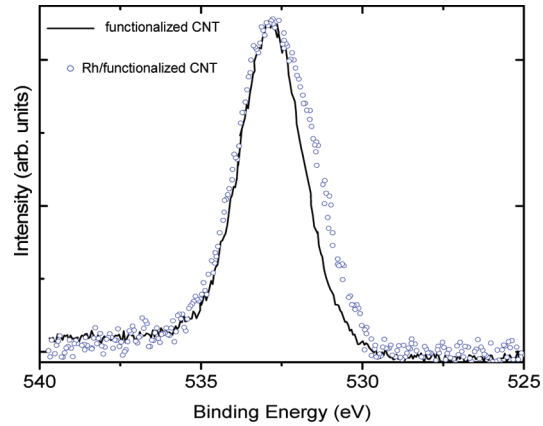

Figure 5. Comparison of the O 1s spectra recorded on oxygen-plasma-treated CNTs and after 5 Å Rh deposition.

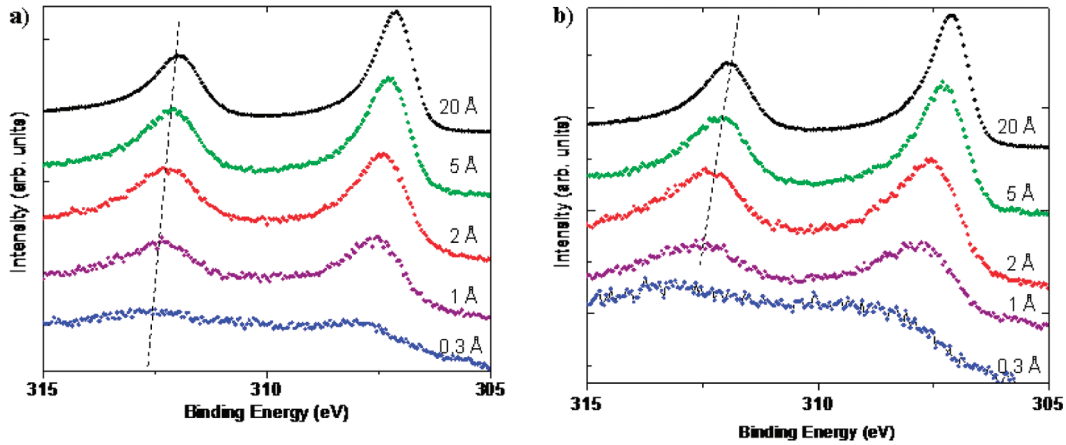

Figure 6. Evolution of the Rh 3d photoelectron spectra for increasing nominal amount of evaporated Rh onto (a) pristine CNTs and (b) plasma-functionalized CNTs (figures indicate nominal thickness of evaporated Rh in Å, as explained in the text).

more stable than a Rh atom and an oxygenated vacancy separated on the graphene surface). This is not such a high energetic cost and is lower than for other metals we have examined,[22] particularly given that one of the oxygen atoms ends up with only a single Rh−O bond as a result. Thus, in the presence of larger Rh clusters, such oxygen displacement from oxygenated vacancies could easily become favorable.

In the presence of environmental oxygen, the calculations again show similarities and differences between Rh and Ti. As for Ti, a single Rh atom on a graphene surface bonds to an incoming O_2 molecule, dilating the Rh−C bonds to 2.55 Å, and forming a distorted RhO_2 molecule with Rh−O bonds of 1.73 Å and O−Rh−O bond angle of 128.2° (as compared to 1.70 Å and 161.5° for an isolated gas-phase RhO_2 molecule). However, unlike Ti, the binding energy is much weaker (2.71 eV per O_2 molecule, as compared to 8.59 eV for Ti).[22] Hence, particularly once clustered, Rh may be less environmentally oxygen sensitive than Ti.

The evolution of the Rh 3d core-level spectrum for a sequence of Rh evaporations onto pristine and plasma-treated CNTs is shown in Figure 6. Comparing spectra recorded on both samples in the onset of the Rh evaporation, they show very different profiles, possibly due to the formation of Rh−O and the presence of smaller clusters. Increasing the amount of nominal Rh evaporation (*i.e.*, cluster size) shifts the spectra toward lower binding energies (see dotted lines in Figure 6). Three factors associated with cluster size can contribute to the core-level binding energy shift: initial-state effects associated with changes in the local electronic structure (valence electron configuration), final-state effects due to changes in the relaxation process (extra-atomic response to the positively charged photohole), and cluster charging.[26,27] The influence of each of these factors on the core-level binding energy depends on the nature of the cluster (*i.e.*, the chemical composition, shape, size, and area of interaction with the support) and on the nature of the support. On the basis of current photoemission results alone, we cannot unambiguously differentiate between initial- and final-state effects.

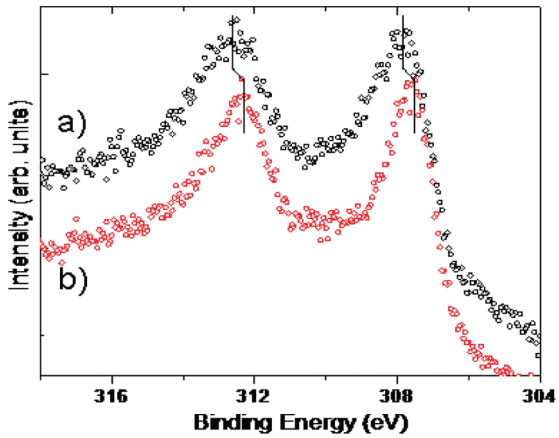

Figure 7. Comparison of the Rh 3d photoelectron spectra recorded after 1 Å of nominal evaporated Rh onto (a) plasma-functionalized and (b) pristine CNTs.

A comparison with the particle size distribution observed in HRTEM (Figure 4) can explain some of the peak behavior. In photoemission final effects, the photohole left behind by the emitted photoelectron leads to a net positive charge on the cluster. The Coulomb interaction reduces the kinetic energy of the photoelectron, which therefore appears at a higher binding energy in the spectrum. This effect increases with decreasing particle size and is affected by the conductivity of the substrate.[29] In the plasma-treated sample, we see a smaller average particle size (Figure 4), which will thus leads to the observed shift in the Rh 3d peak to higher binding energies. However, the increased peak broadening (Figure 7) in this case cannot be explained by the same particle size effect because the particle size distribution for the plasma-treated samples is narrower than that for the pristine samples (Figure 4).

Nevertheless, the smaller cluster size can still be the cause of this peak broadening. Independent of the photoemission process, the initial-state effects are related to

changes in the electronic configuration due to different chemical states (*e.g.*, formation of Rh−O bonds) and quantum size effects due to limited cluster dimensions.[28] The larger broadening in the XPS lines, at the onset of deposition (*i.e.*, for small clusters), reflects the reduced coordination of clusters surface atoms and its effect on the core-hole lifetime; the broadening drops for increasing cluster size. Therefore, it can be suggested that the broadening in the line is caused by both the presence of smaller clusters and the formation of Rh−O−C bonds at the Rh−CNT interface.

CONCLUSIONS

Rhodium exhibits quite different surface behavior on CNTs as compared to Ti. It forms discrete highly crystalline faceted particles rather than a continuous amorphous layer, despite showing similar strong surface interaction. Rh has a higher surface mobility than Ti, but lower than other metals such as Au and Pt, and interacts less strongly with oxygen. Nonetheless, it appears to be able to scavenge oxygen from oxygenated vacancy sites. All of these properties would suggest a material capable of forming good metal contacts with the nanotube surface. The possibility to activate the formation of carbon layers has to be cared for in order to avoid poisoning at the contacts.

Oxygen-plasma treatment in a RF plasma grafts oxygen to the CNT surface, creating cluster nucleation sites. Subsequent Rh deposition results in smaller clusters with more uniform size distribution than on pristine tubes. The absence of new features in the C 1s and Rh core-level XPS spectra demonstrates the absence of chemical reaction at the Rh cluster−CNT interface. We note that the presence of oxygenated vacancies inhibits any spin associated with the Rh, and this will probably mean that the unusual magnetic properties predicted for monolayer Rh will be quenched in the presence of defects.[11] In order to avoid size effects in the contacts that could imply refrain electrical charge injection, it is recommended to evaporate more than 20 Å of Rh.

METHODS

The Rh−CNT samples were prepared using commercially available MWCNTs synthesized using the arc discharge method.[29] Nominal amounts of 0.3, 1, 2, 5, and 20 Å of Rh were evaporated onto the CNT samples, as calibrated using a quartz microbalance. Hence, Rh thicknesses quoted within the text refer to the amount of Rh deposited on the quartz surface under identical experimental conditions, rather than any local measurement of Rh deposition on the sample itself. The oxygen-plasma treatment was performed using an inductively coupled RF plasma (13.56 MHz).[30] The CNT powder was placed inside a plasma glow discharge, which was generated at a power setting of 15 W, and treated at an oxygen pressure of 0.1 Torr for a duration of 60 s. Samples were transferred to the metal deposition chamber.

The elemental and chemical characterization of the samples was performed by XPS. The fundamental phenomenon underlying the XPS is the photoelectric effect that describes the ejection of electrons from a surface when photons impinge upon it. The kinetic energy (or binding energy) of the ejected electron is characteristic of each element and its chemical state. Hence, XPS can provide chemical bonding information. The XPS measurements were performed at the BW2 beamline at Hasylab (Hamburg) using a photon energy of 3.5 keV,[31−33] and possible photon energy drift during the measurements was removed by monitoring a Au $4f_{7/2}$ reference signal at 84.00 eV binding energy. Reference spectra were measured before and after each core-level data sets for all samples. At 3.5 keV photon energy, the escape depth of the primary photoelectrons that contributes to the C 1s photoelectron peak is about 50 Å;[34] consequently, we restricted the Rh evaporation to amounts that allow detection of photoelectrons emitted from atoms localized at the Rh−CNT interface region. For XPS analysis, the samples were prepared *in situ* by electron beam evaporation of Rh onto CNTs supported on a conductive carbon tape. The base pressure in the analyzer chamber of beamline BW2 is 1×10^{-10} mbar.

Analysis of individual metal particles and the determination of their size distribution and dispersion were performed by high-resolution TEM using a Philips CM30 FEG microscope, operated at 200 kV electron energy.

Density functional calculations were performed using the AIMPRO code,[35,36] under the local spin density approximation (LSDA) in the supercell approach. All atomic positions as well as system spin were optimized in a 8×8 unit cell of graphene (*i.e.*, 128 carbon atoms). A single *k*-point sampling scheme was used. Hartwigsen, Goedecker, and Hutter pseudopotentials were used,[37] with the Rh $4s^2$ and $4p^6$ electrons treated explicitly to avoid the need for nonlinear core corrections. Gaussian basis functions centered at the atomic cores were used to construct the many-electron wave function. We can write these functions using three orbital symbols, where for each symbol all angular momenta are allowed up to maximum p ($l = 0, 1$), d ($l = 0, 1, 2$), and f ($l = 0, 1, 2, 3$). Following this nomenclature, the basis sets used are pdddp for carbon atoms, ddfd for rhodium atoms, and dddd for oxygen atoms. Charge density oscillations during the self-consistency cycle were damped using a Fermi occupation function with $k_BT = 0.04$ eV. In the energetic analysis that follows, the binding energy is defined as the difference in energy between the relaxed combined system and isolated perfect graphite sheet and isolated single metal atoms. The isolated atom was chosen as our metal reference state because, experimentally, the metal atoms are thermally evaporated onto the tube surface and arrive mostly as individual atoms rather than preformed clusters.

To evaluate the accuracy of our calculations, we examined bulk Rh and isolated Rh clusters of up to four atoms in the gas phase (bulk Rh and isolated clusters, Rh_n, $n = 1,4$). Our calculated bulk cohesive energy is 7.81 eV/atom, with a unit cell length of 3.77 Å, in good agreement with previous DFT/LDA calculations (8.29 eV/atom and 3.81 Å)[38] and as to be expected for LDA, slightly higher binding than experiment (5.71 eV/atom and 3.80 Å).[39] The spin-state and ground-state structure of the Rh_n cluster ($n = 1,4$) agrees with previous calculations in the literature.[40]

Acknowledgment. This work is financially supported by the Belgian Program on Interuniversity Attraction Pole (PAI 6/08), ARC-UMONS, by the EU FP6 project STREP "nano2hybrids", Reference 003311, and by DESY and the European Commission under Contract RII3-CT 2004-506008 (IASFS). J.G. is a research associate of NFSR (Belgium).

REFERENCES AND NOTES

1. Javey, A.; Kim, H.; Brink, M.; Wang, Q.; Ural, A.; Guo, J.; McIntyre, P.; McEuen, P.; Lundstrom, M.; Dai, H. J. High-*k* Dielectrics for Advanced Carbon-Nanotube Transistors and Logic Gates. *Nat. Mater.* **2002**, *1*, 241–246.

2. Javey, A.; Guo, J.; Wang, Q.; Lundstrom, M.; Dai, H. J. Ballistic Carbon Nanotube Field-Effect Transistors. *Nature* **2003**, *424*, 654–657.
3. Wind, S. J.; Appenzeller, J.; Martel, R.; Derycke, V.; Avouris, P. Vertical Scaling of Carbon Nanotube Field-Effect Transistors Using Top Gate Electrodes. *Appl. Phys. Lett.* **2002**, *80*, 3817–3819.
4. Mann, D.; Javey, A.; Kong, J.; Wang, Q.; Dai, H. J. Ballistic Transport in Metallic Nanotubes with Reliable Ohmic Contacts. *Nano Lett.* **2003**, *3*, 1541–1544.
5. Krstic, V.; Kim, G. T.; Park, J. G.; Suh, D. S.; Park, Y. W.; Roth, S.; Burghard, M. Role of the Metal in Contacting Single-Walled Carbon Nanotubes. *AIP Conf. Proc.* **2000**, *544*, 367–370.
6. Vitale, V.; Curioni, A.; Andreoni, W. J. Metal−Carbon Nanotube Contacts: The Link between Schottky Barrier and Chemical Bonding. *J. Am. Chem. Soc.* **2008**, *130*, 5848–5849.
7. Nemec, N.; Tomanek, D.; Cuniberti, G. Contact Dependence of Carrier Injection in Carbon Nanotubes: An *Ab Initio* Study. *Phys. Rev. Lett.* **2006**, *96*, 076802-2.
8. Kim, W.; Javey, A.; Tu, R.; Cao, J.; Wang, Q.; Dai, H. Electrical Contacts to Carbon Nanotubes down to 1 nm in Diameter. *Appl. Phys. Lett.* **2005**, *87*, 173101-3.
9. Larciprete, R.; Lizzit, S.; Petaccia, L.; Goldoni, A. NO_2 Decomposition on Rh Clusters Supported on Single-Walled Carbon Nanotubes. *Appl. Phys. Lett.* **2006**, *88*, 243111-3.
10. Methfessel, M.; Henning, D.; Scheffler, M. Trends of the Surface Relaxations, Surface Energies, and Work Functions of the 4d Transition Metals. *Phys. Rev. B* **1992**, *46*, 4816–4829.
11. Krüger, P.; Parlebas, J. C.; Moraitis, G.; Demangeat, C. Magnetism of Epitaxial Ru and Rh Monolayers on Graphite. *Comput. Mater. Sci.* **1998**, *10*, 265–268.
12. Zhao, J.-X.; Ding, Y.-H. Theoretical Study of the Interactions of Carbon Monoxide with Rh-Decorated (8,0) Single-Walled Carbon Nanotubes. *Mater. Chem. Phys.* **2008**, *110*, 411–416.
13. Tracz, A.; Wegner, J.; Rabe, J. P. Kinetics of Surface Roughening *via* Pit Growth during the Oxidation of the Basal Plane of Graphite. 1. Experiments. *Langmuir* **1993**, *9*, 3033–3038.
14. Ionescu, R; Espinosa, E. H.; Sotter, E.; Llobet, E.; Vilanova, X.; Correig, X.; Felten, A.; Bittencourt, C.; Van Lier, G.; Charlier, J.-C.; Pireaux, J.-J. Oxygen Functionalisation of MWNT and Their Use as Gas Sensitive Thick-Film Layers. *Sens. Actuators, B* **2006**, *113*, 36–46.
15. Carlsson, J. M.; Hanke, F.; Linic, S.; Scheffler, M. Two-Step Mechanism for Low-Temperature Oxidation of Vacancies in Graphene. *Phys. Rev. Lett.* **2009**, *102*, 166104-4.
16. Chen, C. L.; Liang, B.; Ogino, A.; Wang, X. K.; Nagatsu, M. Oxygen Functionalization of Multiwall Carbon Nanotubes by Microwave-Excited Surface-Wave Plasma Treatment. *J. Phys. Chem. C* **2009**, *113*, 7659–7665.
17. Tseng, W. S.; Tseng, C. Y.; Chuang, P. K.; Lo, A. Y.; Kuo, C. T. A High Efficiency Surface Modification Process for Multiwalled Carbon Nanotubes by Electron Cyclotron Resonance Plasma. *J. Phys. Chem. C* **2008**, *112*, 18431–18436.
18. Desai, S. C.; Hewaparakrama, K. P.; Jayasinghe, C.; Mast, D.; Pradhan, B. K.; Sumanasekera, G. U. Desorption Kinetics of Oxygen in Plasma Treated SWNTs by *In Situ* Thermoelectric Power Measurements. *Nanotechnology* **2008**, *19*, 095507–095511.
19. Suarez-Martinez, I.; Felten, A.; Pireaux, J.-J.; Bittencourt, C.; Ewels, C. P. Transition Metal Deposition on Graphene and Carbon Nanotubes. *J. Nanosci. Nanotechnol.* **2009**, *9*, 6171–6175.
20. Krasheninnikov, A.; Lehtinen, P. O.; Foster, A. S.; Pyykko, P.; Nieminen, R. M. Embedding Transition-Metal Atoms in Graphene: Structure, Bonding, and Magnetism. *Phys. Rev. Lett.* **2009**, *102*, 126807-4.
21. Durgun, E.; Dag, S.; Bagci, V. M. K.; Gulseren, O.; Yildirim, T.; Ciraci, S. Systematic Study of Adsorption of Single Atoms on a Carbon Nanotube. *Phys. Rev. B* **2003**, *67*, 20140-4.
22. Felten, A.; Suarez-Martinez, I.; Ke, X.; Van Tendeloo, G.; Ghijsen, J.; Pireaux, J.-J.; Drube, W.; Bittencourt, C.; Ewels, C. P. The Role of Oxygen at the Interface between Titanium and Carbon Nanotubes. *ChemPhysChem* **2009**, *10*, 1799–1804.
23. Suarez-Martinez, I.; Bittencourt, C.; Ke, X.; Felten, A.; Pireaux, J.-J.; Ghijsen, J.; Drube, W.; Van Tendeloo, G.; Ewels, C. P. Probing the Interaction between Gold Nanoparticles and Oxygen Functionalized Carbon Nanotubes. *Carbon* **2009**, *47*, 1549–1554.
24. Felten, A.; Ghijsen, J.; Pireaux, J.-J.; Johnson, R. L.; Whelan, C. M.; Liang, D.; Van Tendeloo, G.; Bittencourt, C. Effect of Oxygen RF-Plasma on Electronic Properties of CNTs. *J. Phys. D* **2007**, *40*, 7379–7382.
25. Goldoni, A.; Baraldi, A.; Comelli, G.; Esh, F.; Larciprete, R.; Lizzit, S.; Paolucci, G. Morphology and Magnetic Properties of Thin Films of Rh on Highly Oriented Pyrolitic Graphite. *Phys. Rev. B* **2000**, *63*, 035405-8.
26. Boyen, H.-G.; Ethirajan, A.; Kästle, G.; Weigl, F.; Ziemann, P.; Schmid, G.; Garnier, M. G.; Büttner, M.; Oelhafen, P. Alloy Formation of Supported Gold Nanoparticles at Their Transition from Clusters to Solids: Does Size Matter? *Phys. Rev. Lett.* **2005**, *94*, 016804.
27. Boyen, H.-G.; Herzog, T.; Kästle, G.; Weigl, F.; Ziemann, P.; Spatz, J. P.; Möller, M.; Wahrenberg, R.; Garnier, M. G.; Oelhafen, P. X-ray Photoelectron Spectroscopy Study on Gold Nanoparticles Supported on Diamond. *Phys. Rev. B* **2002**, *65*, 075412.
28. Sun, Y.; Pan, J. S.; Tao, J. G.; Nie, Y. G.; Huan, C. H. A.; Zhang, Z.; Chai, J. W.; Li, D.; Wang, S. J.; Sun, C. Q. Size Dependence of the $2p_{3/2}$ and $3d_{5/2}$ Binding Energy Shift of Ni Nanostructures: Skin-Depth Charge and Energy Trapping. *J. Phys. Chem. C* **2009**, *113*, 10939–10946.
29. http://www.mercorp.com.
30. Felten, A.; Bittencourt, C.; Pireaux, J.-J.; Van Lier, G.; Charlier, J.-C. Radio-Frequency Plasma Functionalization of Carbon Nanotubes Surface O_2, NH_3, and CF_4 Treatments. *J. Appl. Phys.* **2005**, *98*, 074308.
31. Drube, W.; Schulte-Schrepping, H.; Schmidt, H.-G.; Treusch, R.; Materlik, G. Design and Performance of the High-Flux/High-Brightness X-ray Wiggler Beamline BW2 at HASYLAB. *Rev. Sci. Instrum.* **1995**, *66*, 1668–1670.
32. Schulte-Schrepping, H.; Heuer, J.; Hukelmann, B. Adaptive Indirectly Cooled Monochromator Crystals at HASYLAB. *J. Synchrotron Radiat.* **1998**, *5*, 682–684.
33. Drube, W.; Grehk, T. M.; Treusch, R.; Materlik, G. Tunable High-Energy X-ray Photoemission. *J. Electron Spectrosc.* **1998**, *88*, 683–687.
34. *Surface Analysis by Auger and X-ray Photoelectron Spectroscopy*; Briggs D., Grant J. T., Eds.; IM Publications: Chichester, U.K., 2003.
35. Rayson, M. J.; Briddon, P. R. Rapid Iterative Method for Electronic-Structure Eigenproblems Using Localised Basis Functions. *Comput. Phys. Commun.* **2007**, *178*, 128–134.
36. Briddon, P. R.; Jones, R. LDA Calculations Using a Basis of Gaussian Orbitals. *Phys. Status Solidi B* **2000**, *217*, 131–171.
37. Hartwigsen, C.; Goedecker, S.; Hutter, J. Relativistic Separable Dual-Space Gaussian Pseudopotentials from H to Rn. *Phys. Rev. B* **1998**, *58*, 3641–3662.
38. Stokbro, K. Mixed Ultrasoft/Norm-Conserved Pseudopotential Scheme. *Phys. Rev. B* **1996**, *53*, 6869–6872.
39. *CRC Handbook of Chemistry and Physics*; Lide, D. R., Ed.; CRC Press: Boca Raton, FL, 1994.
40. Wang, L.; Ge, Q. Studies of Rhodium Nanoparticles Using the First Principles Density Functional Theory Calculations. *Chem. Phys. Lett.* **2002**, *366*, 368–376.